

## Characterization of forced response of density stratified reacting wake

Samadhan A. Pawar, Raman I. Sujith, Benjamin Emerson, and Tim Liewen

Citation: *Chaos* **28**, 023108 (2018);

View online: <https://doi.org/10.1063/1.5006453>

View Table of Contents: <http://aip.scitation.org/toc/cha/28/2>

Published by the [American Institute of Physics](#)

---

---

Welcome to a

Smarter Search 

PHYSICS  
TODAY

with the redesigned  
*Physics Today Buyer's Guide*

Find the tools you're looking for today!

# Characterization of forced response of density stratified reacting wake

Samadhan A. Pawar,<sup>1,a)</sup> Raman I. Sujith,<sup>1</sup> Benjamin Emerson,<sup>2</sup> and Tim Liewen<sup>2</sup>

<sup>1</sup>Department of Aerospace Engineering, Indian Institute of Technology Madras, Chennai 600036, India

<sup>2</sup>Department of Aerospace Engineering, Georgia Institute of Technology, Atlanta, Georgia 30332, USA

(Received 25 September 2017; accepted 23 January 2018; published online 8 February 2018)

The hydrodynamic stability of a reacting wake depends primarily on the density ratio [i.e., ratio of unburnt gas density ( $\rho_u$ ) to burnt gas density ( $\rho_b$ )] of the flow across the wake. The variation of the density ratio from high to low value, keeping  $\rho_u/\rho_b > 1$ , transitions dynamical characteristics of the reacting wake from a linearly globally stable (or convectively unstable) to a globally unstable mode. In this paper, we propose a framework to analyze the effect of harmonic forcing on the deterministic and synchronization characteristics of reacting wakes. Using the recurrence quantification analysis of the forced wake response, we show that the deterministic behaviour of the reacting wake increases as the amplitude of forcing is increased. Furthermore, for different density ratios, we found that the synchronization of the top and bottom branches of the wake with the forcing signal is dependent on whether the mean frequency of the natural oscillations of the wake ( $f_n$ ) is lesser or greater than the frequency of external forcing ( $f_f$ ). We notice that the response of both branches (top and bottom) of the reacting wake to the external forcing is asymmetric and symmetric for the low and high density ratios, respectively. Furthermore, we characterize the phase-locking behaviour between the top and bottom branches of the wake for different values of density ratios. We observe that an increase in the density ratio results in a gradual decrease in the relative phase angle between the top and bottom branches of the wake, which leads to a change in the vortex shedding pattern from a sinuous (anti-phase) to a varicose (in-phase) mode of the oscillations. *Published by AIP Publishing.*

<https://doi.org/10.1063/1.5006453>

In most of the practical combustion systems, the incoming flow to a combustor is preheated to a higher temperature before stabilization of a flame in the bluff body wake. The hydrodynamic stability has a strong dependence on the density ratio across the wakes. As a result, the hydrodynamic stability of preheated reacting wakes (flame) differs substantially from non-preheated ones. One important distinction is that most non-preheated reacting wakes are convectively unstable, whereas the highly preheated wakes are globally unstable.<sup>1</sup> The interaction of such reacting wakes with the acoustic field in the combustor is responsible for the generation of a high-amplitude acoustic field of the combustor. Such oscillations are often referred to as thermoacoustic instability. The onset of these instabilities is undesirable for the combustor operation and needs to be avoided. Hence, it is important to study the effect that a change in the density of the incoming flow, due to preheating, has on the hydrodynamic stability of the reacting wake and the interaction of such reacting wakes with acoustics of the combustor. Such a characterization of the reacting wake was performed by Emerson and Liewen<sup>2</sup> by harmonically forcing the reacting wake at different conditions of density stratification. Hitherto, the response of such wakes to the external forcing was mostly based on the measures from linear theory, e.g., coherence, cross-correlation coefficient, and Fourier phase. Since the response of reacting wakes to external forcing is a nonlinear phenomenon, additional insights can be gained by the use of tools from

recurrence plot (RP) analysis and synchronization theory. With the help of these measures, we propose a framework to analyze the forced response of the reacting wake for different conditions of the flow and the forcing parameters.

## I. INTRODUCTION

Bluff bodies play a significant role in the stabilization of the flame inside the combustors of high performance systems such as ramjets, afterburners of turbojet engines, and land based gas turbine engines.<sup>3–5</sup> The flames are stabilized in the low velocity recirculation zone created downstream of the bluff body.<sup>6</sup> Bluff body stabilized flames are further susceptible to other combustion phenomena such as flashback, blowoff,<sup>7</sup> and thermoacoustic instability.<sup>8–10</sup>

The flow field of a bluff body mainly consists of three topological features: boundary layers, separating shear layers, and wake.<sup>11</sup> Hydrodynamic instabilities of these features play a dominant role in the aforementioned thermoacoustic instability of confined combustors.<sup>7</sup> When a high Reynolds number flow is established over the bluff body, two shear layers, consisting of high speed cold reactant flow on one side and low speed hot combustion products on the other side, are formed outside the recirculation zone.<sup>12</sup> These shear layers are hydrodynamically unstable, which results in the formation of large scale vortical structures that are further convected downstream of the bluff body. These convecting vortical structures wrinkle the flame and modulate its

<sup>a)</sup>Author to whom correspondence should be addressed: samadhanpawar@iitm.ac.in

heat release rate.<sup>12</sup> The modulated heat release rate adds energy to the acoustic field,<sup>13</sup> which may in turn excite the hydrodynamically unstable shear layers and thus close the feedback loop necessary for the onset of thermoacoustic instability. When the instantaneous phases of these coupled processes demonstrate a perfect phase-locking,<sup>14,15,69</sup> the pressure oscillations in the system may attain a high amplitude, self-sustained state known as thermoacoustic instability. The presence of thermoacoustic instability is undesirable for combustion systems and has been an obstacle to the development of high performance engines over decades.<sup>10,16</sup>

The onset of thermoacoustic instability involves a mutual interaction between various processes of the thermoacoustic system such as acoustic oscillations in the duct, heat release rate fluctuations in the flame, hydrodynamics of the underlying flow field, and entropy waves.<sup>17</sup> The complexity in the analysis of thermoacoustic instability is reduced by separately studying the role of individual dynamical systems of the combustor which couple to generate these instabilities.<sup>18</sup> In one such approach, the flame is subjected to externally imposed velocity perturbations, and the response dynamics of the driven flame fluctuations are measured for different parameters of the external forcing.<sup>10</sup> Most of the studies on forcing in thermoacoustic systems are based on harmonic forcing.<sup>19–22</sup> Harmonic forcing is further classified into longitudinal<sup>23,24</sup> or transverse,<sup>25,26</sup> depending on whether the forcing is in the streamwise or the cross-stream direction, respectively. In this paper, we study the response of a bluff body stabilized reacting wake to an externally applied longitudinal harmonic forcing during the stable operation of the combustor. In this case, stable operation means a stable thermoacoustic system (i.e., weak feedback between flame dynamics and duct acoustics), not a hydrodynamically stable flow.

The forced response of the flame dynamics is further dependent on the global hydrodynamic stability of the underlying flow field of the combustor.<sup>2</sup> For a non-reacting wake, the flow field is either globally stable or globally unstable,<sup>27</sup> depending on the Reynolds number. Global instability in high Reynolds number wakes manifests as asymmetric Bénard-von Kármán vortex shedding.<sup>28,29</sup> Regardless of the global stability of the flow, the separating shear layers will always be convectively unstable (due to Kelvin-Helmholtz instability), such that flows with globally stable wakes will be convectively unstable. Therefore, we classify the hydrodynamic stability of the flow in this study as either convectively or globally unstable modes.

The introduction of combustion alters the global stability of the bluff body wake field<sup>30,31</sup> through the addition of the density ratio ( $\rho_u/\rho_b$ ) as another control parameter.<sup>1,32,33</sup> Density ratios far from unity tend to stabilize the global mode, rendering the wake convectively unstable.<sup>27</sup> This is the situation in wakes of premixed combustors with highly exothermic combustion and/or little preheat of the reactant mixture. At density ratios closer to 1 (where the density ratio equal to 1 represents a non-reacting wake), high Reynolds number wakes are globally unstable,<sup>32</sup> which happens due to weak exothermic combustion and/or high degree preheating of the reactant mixture. When the density ratio is decreased

from one extreme to the other in a high Reynolds number flow, the transition from convective to global instability is observed to be not sudden; it happens gradually via intermittency.<sup>1,34</sup>

Convectively unstable and globally unstable flows exhibit substantially different forced response characteristics. Convectively unstable flows are seemingly linear amplifiers,<sup>27</sup> i.e., such flows display response to the both low and high values of the forcing amplitudes. Therefore, the effect of forcing is most prominent in convectively unstable flows, such as the shear layers separating from a bluff body. In contrast, globally unstable flows exhibit a nonlinear response to external disturbances.<sup>27</sup> These flows will tend to oscillate at their own natural frequency in the presence of low amplitude external forcing but may respond to the forcing when the amplitude of forcing is large. In such a situation, a nonlinear phenomenon of frequency-locking may be observed for the conditions of high amplitude forcing.<sup>35,36</sup> During the frequency-locking condition, the frequency associated with the global mode oscillations in the wake locks-in with that of the external forcing. Furthermore, to note that although the response of the forced wake to the forcing could be linear or nonlinear, the underlying flow being turbulent is highly nonlinear and inherently complex.

The effect of forcing on non-reacting wakes has been widely studied.<sup>37–42</sup> In the absence of forcing, the vortex shedding frequency exhibits a certain amount of phase noise that is centered around a particular frequency, often parameterized by a Strouhal number. The application of forcing results in synchronized shedding of vortices at the frequency of forcing. The locking of this forcing frequency with the frequency of vortex shedding depends on the difference between these frequencies and the amplitude of forcing. For larger frequency spacing, a higher value of forcing amplitude is required for the entrainment of these frequencies.<sup>43</sup>

For reacting wakes, the effect of forcing on the dynamics of the flame for high density ratios ( $\rho_u/\rho_b \gg 1$ , convectively unstable flow) and low density ratios ( $\rho_u/\rho_b \rightarrow 1$ , globally unstable) is quite different due to the difference in the stability of the underlying hydrodynamic flow field. The first study to systematically quantify the response of the reacting wake to the harmonic forcing, for different conditions of the density ratio, was performed by Emerson and Lieuwen.<sup>2</sup> They found that although the longitudinal forcing naturally excites the varicose mode (symmetric vortex shedding), the sinuous mode (asymmetric vortex shedding) is the fastest-growing mode downstream of the bluff body wake for a wide range of density ratios when  $f_n \approx f_f$ . When the forcing frequency is near the natural frequency of the global mode, the sensitivity of the external forcing is different for the flame edge fluctuations and for the heat release rate fluctuations. At this condition of forcing, the heat release rate fluctuations are minimum, and the transversely induced flame edge fluctuations are maximum, referred to as resonant amplification.<sup>2</sup> For a fixed value of the forcing amplitude, the increase in the density ratio results in an increase in the region of resonant amplification of the system.<sup>44</sup>

In this paper, we extend the analysis of Emerson and Lieuwen<sup>2,44</sup> and propose a framework to characterize the

forced response of a highly turbulent, density stratified, bluff body stabilized reacting wake using various tools from the dynamical systems theory.<sup>45–48</sup> In the previous studies, the characterization of reacting wakes was based on measures from linear theory.<sup>2,24,49</sup> However, since the response of the reacting wake (or flame) to the external forcing is nonlinear,<sup>50</sup> it is necessary to have a framework to understand the interactions between the signals of forcing and forced response of the wake in a better manner. Recently, for a case of hydrodynamically unstable flow field, Juniper and co-workers used the framework of forced synchronization<sup>51</sup> to study the forced response of a low density jet,<sup>52</sup> a diffusion flame,<sup>53</sup> and a swirl-stabilized flame<sup>54</sup> at different conditions of the forcing parameters. Using the theory of synchronization, they characterized various dynamical states of the forced flame response, such as quasiperiodicity, phase-drifting, phase trapping, and phase locking, which were unnoticed previously in the literature. In a similar manner, here we characterize the various other aspects of the forced wake dynamics such as determinism, symmetry of phase-locking of the top and bottom branches of the wake with the forcing, and the relative phase angle of the vortex shedding from the trailing edges of the bluff body. With this, our study provides an experimental evidence wherein we show that the high-density ratio (convectively unstable) reacting wakes are more receptive to forcing than the low-density ratio (globally unstable) reacting wakes.

## II. DESCRIPTION OF THE EXPERIMENTAL SETUP AND DATA ANALYSIS

The experimental setup consists of two premixed combustors connected in a series. Natural gas and air are premixed and burned in both the combustors. The first combustor acts as a vitiator, whose purpose is to raise the temperature of reactants going into the second combustor. The second combustor consists of a bluff body, with a 2D ballistic shape, used to stabilize the flame in high speed flows. The bluff body span covers the entire combustor width, thus creating a nominal 2D flow in the system. The aspect ratio, the ratio of the height of the bluff body with a width of the second combustor, is 0.15. Quartz glass windows on all four sides of the second combustor provide optical access required for flame imaging. Further details of the experimental facility and its design are provided in the work of Emerson and Lieuwen.<sup>2</sup>

The experimental rig is designed in a manner that allows independent control of the density ratio of the unburned and burned gases present across the flame ( $\rho_u/\rho_b$ ) and the lip velocity of the flow ( $U_{lip}$ ). Another control parameter is the shape of the bluff body which controls the shear layer thickness and also the alignment between the velocity and density profiles; however, we do not focus on this parameter in the present study. Since  $\rho_u/\rho_b = T_b/T_u$ , the density ratio ( $\rho_u/\rho_b$ ) across the flame is varied by varying the preheating temperature of reactants ( $T_u$ ) entering into the second combustor. Secondary fuel and air supply lines are provided in between the two combustors to have flexibility in varying the density ratio and flow velocity in the second combustor. Thus, the inlet temperature to the second combustor (after vitiation in the first combustor and after the addition of secondary air and fuel) is varied from 770 K to 1200 K. Thus, the density ratio can be varied systematically aiding in the study of the growth rate of the hydrodynamic global mode in the system. As we sweep the density ratio from a low ( $\rho_u/\rho_b = 1.7$ ) to a high ( $\rho_u/\rho_b = 2.4$  and  $3.2$ ) value, the flow dynamics gradually transition from a globally unstable [Fig. 1(a)] to a convectively unstable [Figs. 1(c) and 1(d)] mode through intermittency [Fig. 1(b)]. During intermittency ( $\rho_u/\rho_b \approx 2$ ), flow dynamics fluctuate between convectively unstable and globally unstable modes in an apparently random manner. The equivalence ratio and the adiabatic flame temperature in the main combustor were maintained in the range of  $0.7 < \phi < 0.75$  and  $1950 < T_b < 2030$  K, respectively. Great care was taken to operate this combustor well away from the boundaries of blowoff of the flame, where additional flame and flow dynamics can occur.<sup>7,55,56</sup>

Two loudspeakers are mounted on the tubes placed 1 m upstream of the second combustor. The harmonic signal generated using a function generator is amplified and then fed to drive the speakers. As the first transverse mode of the second combustor is 5000 Hz, the multi-dimensional disturbances generated in the system are evanescent and decay quickly. Thus, the acoustic excitation in the second combustor is effectively planar. In all experiments, the forcing frequency ( $f_f$ ) is fixed at a constant value of 515 Hz and the natural frequency of the global mode is varied across this forcing frequency. To achieve this, the lip velocity of the flow ( $U_{lip}$ ) is varied in such a way that the mean frequency of natural oscillations ( $f_n$ ) in the flame is less than, equal to, or greater than  $f_f$ . This has the additional effect of increasing the global mode limit cycle amplitude as the ratio  $f_n/f_f$  is increased.

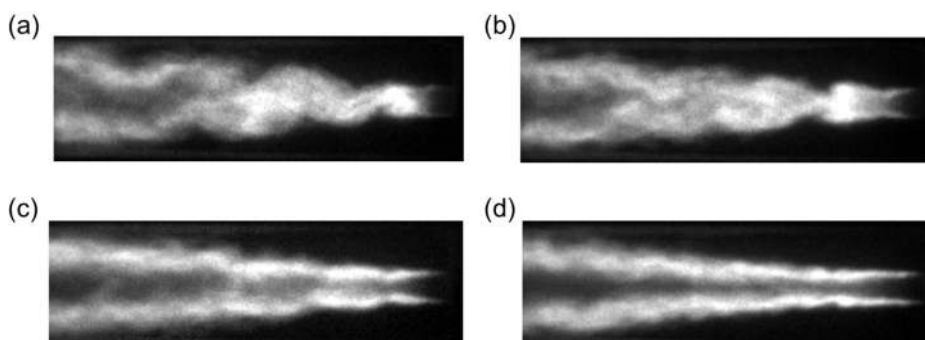


FIG. 1. (a)–(d) The instantaneous CH\* chemiluminescence images of the unforced bluff-body stabilized flame acquired during different values of density ratio such as  $\rho_u/\rho_b = 1.7, 2, 2.4,$  and  $3.2$ , respectively. With a change in the density ratio, the reacting wake dynamics changes from (a) a globally unstable to (c) and (d) a convectively unstable mode through (b) an intermittently oscillatory mode.

The line of sight integrated (along with the bluff body span) imaging of flame  $\text{CH}^*$  chemiluminescence is performed at different conditions of the forcing parameters and density ratios. The high speed  $\text{CH}^*$  chemiluminescence images of the flame are captured using a high speed CMOS camera with  $21.7\ \mu\text{m}$  pixels, a sampling frequency of 5000 Hz, and a pixel resolution of  $768 \times 384$ . The exposure time is fixed at  $1/5000\ \text{s}$ . The camera is outfitted with a 135 mm lens at  $f/2.8$ , with a magnification of 1:17.1. The imaging was performed such that a  $286\ \text{mm} \times 80\ \text{mm}$  region of the main combustor is imaged on  $768 \times 215$  pixels. This captured region of the combustor covers the span from the trailing edge of the bluff body to 15 times bluff body diameters downstream. The flame images are captured through a bandpass filter centered at 434 nm, with 90% transmission between 425.5 nm and 442.5 nm. A total of 4000 images are acquired at every value of the control parameter.

### III. RESULTS AND DISCUSSION

In this section, we first compare the dynamics of the flame in the absence of forcing with that in the presence of forcing when the forcing amplitude is high. We subsequently

move our attention to detect the phase-locking (or synchronization) behaviour of the oscillations in the flame (reacting wake) with the forcing signal. Towards this purpose, we compute the local heat release rate fluctuations from the top and bottom halves of the flame at an unforced state ( $A_f=0$ ) and forced at an amplitude of  $A_f=0.02$ . Here,  $A_f = |u'_{lip}(f_f)/(2f_f D)|$  is the normalized amplitude of the forcing obtained from the ratio of unsteady axial velocity at the bluff body lip ( $u'_{lip}$ ) acquired from the PIV measurement (discussed in detail in Ref. 2) to the diameter of the bluff body ( $D$ ), and  $f_f$  is the frequency of periodic forcing.

#### A. Comparison of dynamics of unforced and forced oscillations of the reacting wake

We see from Figs. 2(a)–2(d) that, during the state of unforced oscillations, the flame edge is weakly modulated, wherein the oscillations in the flame are mainly due to the underlying hydrodynamic instability of the reacting flow. In contrast, the forced flame exhibits oscillatory corrugations on both sides of its surface, as seen in Figs. 2(e)–2(h). These wavy patterns in the flame edge are the result of shedding of large scale vortical structures from the trailing edges of the

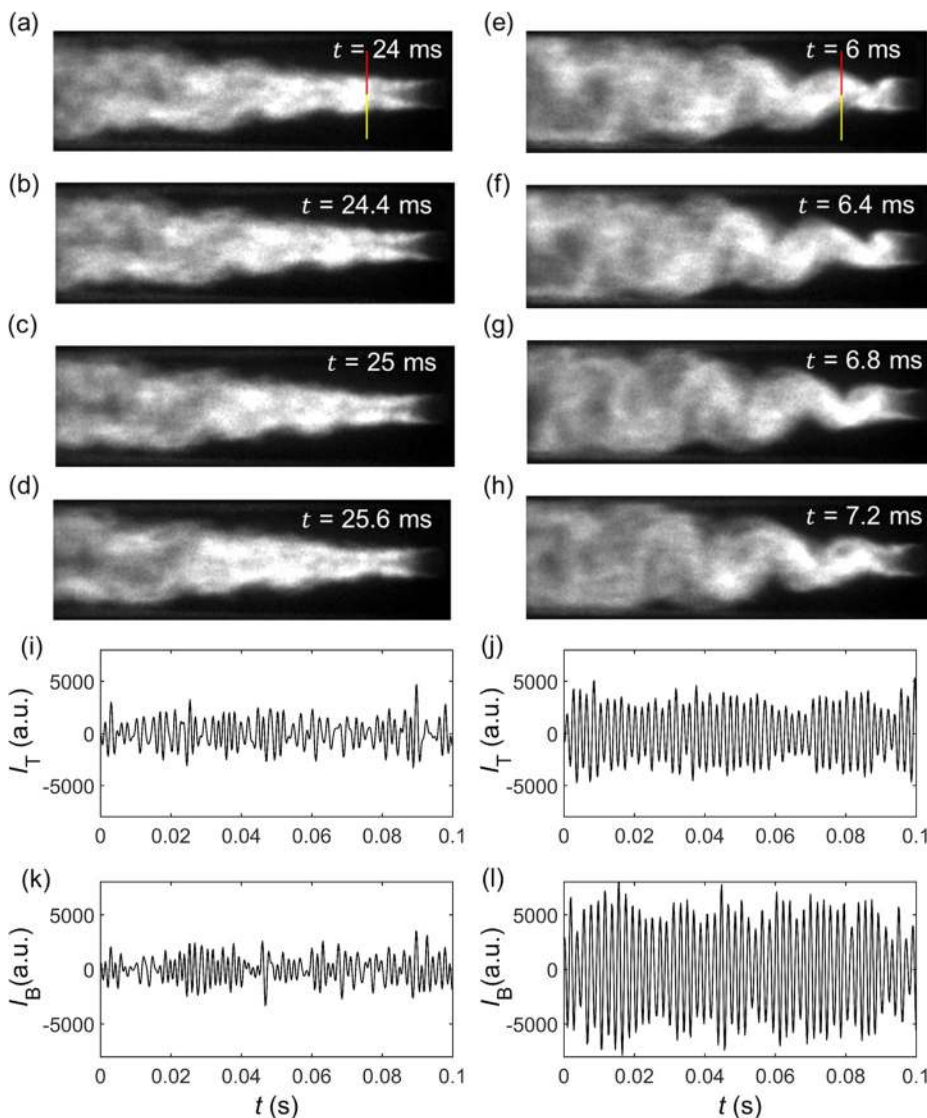


FIG. 2. The instantaneous  $\text{CH}^*$  chemiluminescence images of the flame shown for different time instances of the oscillation cycle captured during (a)–(d) unforced ( $A_f=0$ ) and (e)–(h) forced ( $A_f=0.02$ ) states. The time series of the local heat release rate fluctuations acquired from (i) and (j) top [shown by the red line in (a)] and (k) and (l) bottom [shown by the yellow line in (a)] branches of the flame correspond to  $A_f=0$  and  $A_f=0.02$ , respectively. The parameters that are fixed are  $x/D=3$ ,  $\rho_u/\rho_b=2$ ,  $U_{lip}=40\ \text{m/s}$ , and  $f_n/f_f \approx 1$ . The flow direction is from right to left.

bluff body at a frequency equal to that of the external perturbations (since  $f_n/f_f \approx 1$ ). The vertical lines shown in the flame images [in Figs. 2(a) and 2(e)] with different colors divide the near field of the wake into two equal halves representing the top (red line) and the bottom (yellow line) branches of the flame. The location of the line is chosen at  $x/D = 3$ , which is the same as that of the analysis performed by Emerson and Lieuwen.<sup>2</sup> The instantaneous local heat release rate fluctuations of the top ( $I_T$ ) and bottom ( $I_B$ ) portions of the flame are obtained by summing all the pixel intensities lying along the respective lines. The time series corresponding to these local heat release rate fluctuations ( $I_T$  and  $I_B$ ) for the conditions of unforced state are shown in Figs. 2(i) and 2(k), and forced state are shown in Figs. 2(j) and 2(l). During the unforced state, the oscillations in the flame are aperiodic, which, thereafter, transition to seemingly periodic oscillations due to the application of high amplitude forcing to the flame. We notice an increase in the amplitude of the local heat release rate fluctuations due to forcing.

We, further, characterize the dynamics of these local heat release rate fluctuations in a higher dimensional phase space by using a time-delay embedding theorem proposed by Takens.<sup>57</sup> According to this theorem, a univariate time series can be appropriately embedded into a higher dimensional space if a proper value of the time delay ( $\tau$ ) and the embedding dimension ( $d$ ) are chosen. The optimum value of the time delay can be calculated from the average mutual information,<sup>58</sup> and the minimum embedding dimension can be calculated from the method of false nearest neighbors.<sup>59</sup> A detailed description of the use of Takens' embedding theorem to construct a phase space is found in the work of Abarbanel *et al.*<sup>45</sup> The value of optimum time delay corresponds to the first local minimum of the average mutual information,<sup>58</sup> and the minimum embedding dimension is chosen as the next dimension to the value where the percentage of false nearest neighbors becomes zero for the first time.<sup>59</sup>

Figure 3 shows a three-dimensional reconstructed phase space of the local heat release rate fluctuations obtained from the top ( $I_T$ ) and bottom ( $I_B$ ) branches of the flame

corresponding to unforced [Figs. 3(a) and 3(b)] and forced at  $A_f=0.02$  [Figs. 3(c) and 3(d)] states, respectively. For the unforced case, the attractors of the local flame dynamics show a clutter of trajectories in the phase space due to their aperiodic nature, whereas, during the condition of high amplitude forcing, the phase portraits show a relatively regular behaviour wherein the trajectories are arranged into a distorted oval structure. The scatter of these trajectories in the phase space is a result of the variation in the amplitudes of the periodic oscillations observed in the local heat release rate fluctuations.

The recurrence behaviour of these phase space trajectories is further characterized by using recurrence plots<sup>60</sup> (RP). Recurrence is a property of deterministic dynamical systems<sup>60</sup> in which the recurrent behaviour of a phase space trajectory is captured in a region which has been previously visited by the same trajectory. Recurrence plots help in characterizing various dynamical states such as periodic, quasi-periodic, chaotic, random, and intermittency displayed by the system.<sup>46</sup> In order to construct a recurrence plot, we first need to reconstruct the dynamics of the system in the embedded dimensional phase space (as described previously). Then, the recurrence properties of these phase space trajectories are calculated by finding the distance between any state point of the trajectory and all other points. In practice, since the trajectories in the phase space do not recur exactly at the same point, we need to provide an appropriate value of the threshold to quantify their recurrences. The choice of the threshold further depends on the use of this technique to a particular problem in hand. The equation used for computing the recurrence matrix is given by

$$R_{i,j} = \Theta(\epsilon - \|x_i - x_j\|), \quad (1)$$

where  $i, j = 1, 2, \dots, N_1$ ,  $x_i$  and  $x_j$  are the delayed vectors,  $\epsilon$  is the predefined threshold,  $\|\cdot\|$  is the Euclidian norm, and  $\Theta$  is the Heaviside step function.  $N_1 (= N - (d - 1)\tau)$  is the total number of state points on the phase space trajectory, where  $N$  is the total number of points in the signal,  $d$  is the embedding dimension, and  $\tau$  is the time delay. When the phase space trajectory recurs,  $R_{i,j}$  becomes one and is marked as a

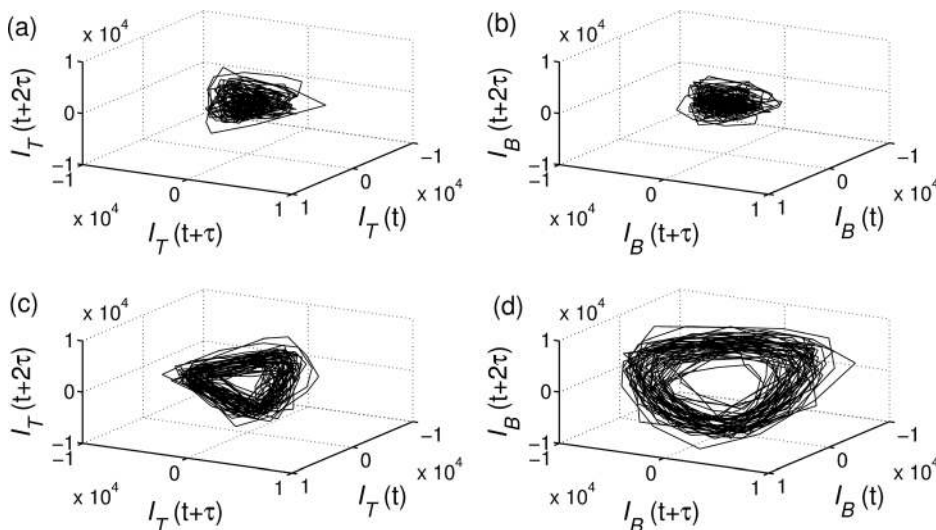


FIG. 3. The reconstructed phase portraits of the local heat release rate fluctuations obtained from the top ( $I_T$ ) and bottom ( $I_B$ ) halves of the flame for the conditions of (a) and (b) unforced ( $A_f=0$ ) and (c) and (d) forced at amplitude  $A_f=0.02$ . The parameters chosen for the reconstruction of the phase space are  $\tau = 0.6$  ms and  $d=6$ . The conditions that are fixed are  $x/D = 3$ ,  $U_{tip} = 40$  m/s,  $f_n/f_f \approx 1$ , and  $\rho_u/\rho_b = 2$ .

black point in the RP. For non-recurring points, the value of  $R_{i,j}$  is zero and is marked as a white point in the RP. Thus, the recurrence plot consists of black and white points, wherein these points are arranged mainly in three orientations as diagonal, horizontal, and vertical.

In Fig. 4, the RPs of the local heat release rate fluctuations obtained from the top and bottom halves of the flame in the absence of forcing [Figs. 4(a) and 4(b)] and in the presence of forcing at  $A_f=0.02$  [Figs. 4(c) and 4(d)] are shown. In the absence of forcing, the RP shows rarer structures of broken lines that are aligned parallel to the main diagonal in the plot. We further note that these short (or broken) diagonal lines are distributed in an apparently random manner. During the state of maximum forcing, the RP appears to be denser with most of the recurrence points aligned along the broken diagonal lines. The lesser the density of the black points, the weaker the recurrence of the phase space trajectory. The existence of short (or broken) diagonal lines in the RPs is an artifact of the presence of either chaotic oscillations<sup>61,62</sup> or higher fluctuations (due to background noise) in the amplitude of periodic signals. In contrast, for white noise signals, the RPs will have only single isolated black points due to their non-recurring behaviour. We subsequently

quantify the recurrence properties of the phase space trajectories when the amplitude of the forcing is varied.

In Figs. 4(e) and 4(f), we plot the variation of two quantitative measures of recurrence<sup>62,63</sup> known as the recurrence rate (%RR) and determinism (%DET), respectively, for different values of the forcing amplitude. The recurrence rate captures the percentage of a total number of state points of a phase space trajectory that recurs inside the threshold. It is calculated as

$$RR = \frac{1}{N_1^2} \sum_{i,j=1}^{N_1} R_{i,j}. \quad (2)$$

On the other hand, determinism captures the percentage of the total number of recurrence points that align in parallel with the main diagonal line in the RP. The determinism is calculated as

$$DET = \frac{\sum_{l=l_{min}}^{N_1} IP(l)}{\sum_{i,j=1}^{N_1} R_{i,j}} \quad (3)$$

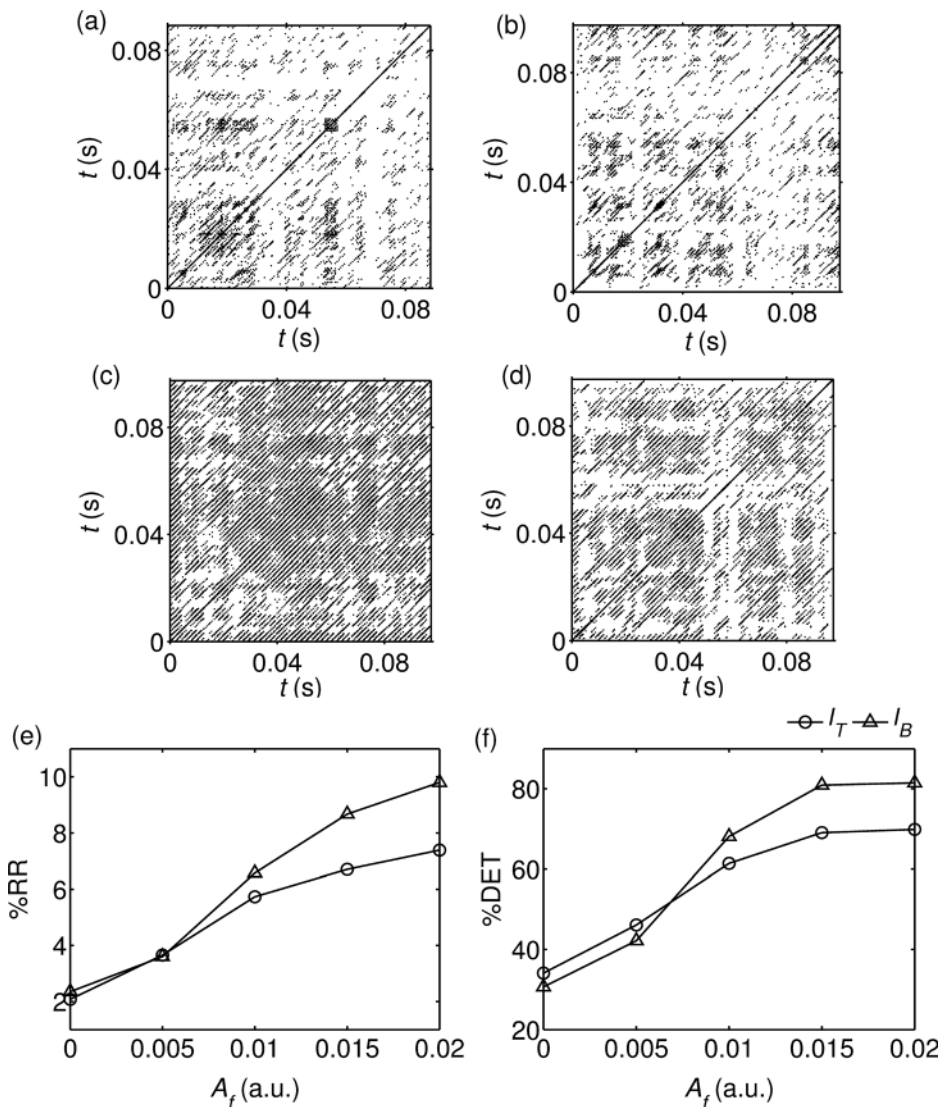


FIG. 4. The recurrence plots of the local heat release rate fluctuations obtained from the top ( $I_T$ ) and bottom ( $I_B$ ) portions of the flame for (a) and (b) the absence of forcing and (c) and (d) the presence of forcing at  $A_f=0.02$ . The variation of recurrence quantification measures such as (e) %RR and (f) %DET is plotted for different values of the forcing amplitude. The conditions that are fixed are  $x/D=3$ ,  $U_{lip}=40$  m/s,  $f_n/f_f \approx 1$ , and  $\rho_u/\rho_b=2$ . Recurrence parameters used for plotting are time delay ( $\tau$ )=0.6 ms, embedding dimension ( $d$ )=6, recurrence threshold ( $\epsilon$ )=20% of the maximum size of the attractor, and the number of data points equal to 1000.

where  $P(l)$  is the histogram of the lengths  $l$  that form diagonal lines in the RP ( $l_{min}=2$  Points). Determinism is a measure of predictability of the dynamical system. It takes higher and lower values for the regular and irregular behaviours of the system dynamics, respectively. We notice an increase in the values of %RR and %DET with an increase in the forcing amplitude. A significantly higher value (as compared to zero) of %DET, during the unforced state, indicates the presence of deterministic or possibly a chaotic behaviour<sup>61,62,64,65</sup> in the local dynamics of the heat release rate signal. The amount of determinism and also periodicity increases with an increase in the forcing amplitude and reaches a maximum value at  $A_f=0.02$ .

## B. Detection of symmetry of forced response of the reacting wake

The dynamics of the forced flame response obtained in terms of local heat release rate fluctuations is further investigated for off-resonance conditions (i.e.,  $f_n/f_f < 1$  and  $f_n/f_f > 1$ ) of forcing. As the heat release rate fluctuations obtained from the top and bottom branches of the flame during the unforced state are broadband [Fig. 6(a-I) and 6(a-II)], the detection of the exact value of natural frequencies of the signal from visual inspection of their frequency spectrums is difficult. Nevertheless, the flow velocity conditions can be maintained in such a way that the mean frequency ( $f_n = (1/2\pi)\langle d\phi/dt \rangle$ , where  $\phi$  is the instantaneous phase of the signal) of the overall selected frequency range of the heat release rate fluctuations, at a given condition of the

frequency ratio, is lower than, nearly equal to, or greater than  $f_f$ . Figure 5 shows the comparison of reconstructed phase portraits of the top and bottom halves of the flame obtained for both conditions of frequency ratios,  $f_n/f_f < 1$  and  $f_n/f_f > 1$ , and four different values of the density ratios (i.e.,  $\rho_u/\rho_b = 1.7, 1.9, 2,$  and  $2.4$ ). Here,  $\rho_u/\rho_b = 1.7$  and  $1.9$  (low density ratios) correspond to the globally unstable flow,  $\rho_u/\rho_b = 2$  (intermediate density ratio) corresponds to the situation of intermittency where the flow dynamics fluctuates between globally and convectively unstable flow characteristics, and  $\rho_u/\rho_b = 2.4$  (high density ratio) corresponds to the convectively unstable flow. We observe in Figs. 5(a) and 5(b) that during the case of low density ratios ( $\rho_u/\rho_b = 1.7$  and  $1.9$ ) and when  $f_n/f_f < 1$ , the phase space trajectories of the top side of the flame display a clutter behaviour, whereas those for the bottom side of the flame show a seemingly regular structure. The situation reverses at these density ratios when  $f_n/f_f > 1$ , wherein the top side of the flame has seemingly a regular behaviour and the bottom side of the flame has a noisy behaviour in the phase space. We hypothesize that small, inherent asymmetry in the geometry may provide a “reference” to the fluid dynamics. This reference allows the flow to respond with a repeatable directionality to its asymmetry. An interesting pair of observations is (a) the repeatability of this phenomenon, which demonstrates a high degree of sensitivity to small geometrical imperfections, and (b) the switching of the directionality of this asymmetry as the frequency ratio ( $f_n/f_f$ ) is varied. Furthermore, we notice a seemingly regular behaviour of

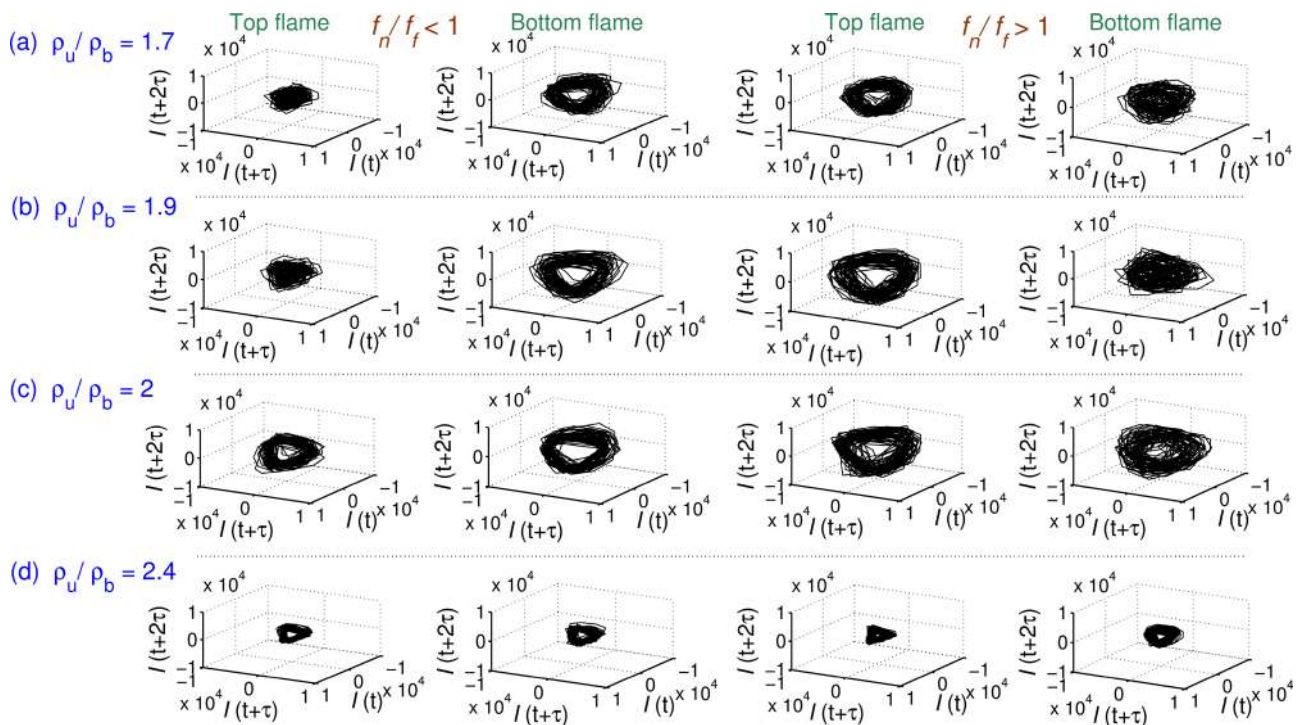


FIG. 5. The reconstructed phase portraits of the local heat release rate fluctuations obtained from the top and bottom sides of the flame are shown for the conditions of two frequency ratios  $f_n/f_f < 1$  and  $f_n/f_f > 1$  and four density ratios (a)  $\rho_u/\rho_b = 1.7$ , (b)  $\rho_u/\rho_b = 1.9$ , (c)  $\rho_u/\rho_b = 2$ , and (d)  $\rho_u/\rho_b = 2.4$ . The flow velocity conditions, for  $\rho_u/\rho_b = 1.7$  ( $U_{ip} = 35$  m/s and  $44$  m/s), for  $\rho_u/\rho_b = 1.9$  ( $U_{ip} = 35$  m/s and  $46$  m/s), for  $\rho_u/\rho_b = 2$  ( $U_{ip} = 34$  m/s and  $46$  m/s), and for  $\rho_u/\rho_b = 2.4$  ( $U_{ip} = 34$  m/s and  $45$  m/s), are chosen such that the conditions of frequency ratios are  $f_n/f_f < 1$  and  $f_n/f_f > 1$ , respectively. The parameters chosen for the reconstruction of the phase space are optimum time delay  $\tau = 0.6$  ms and embedding dimension  $d = 6$ . The conditions that are fixed are  $x/D = 3$  and  $A_f = 0.02$ .

the phase space trajectory for intermediate ( $\rho_u/\rho_b = 2$ ) and sufficiently higher values ( $\rho_u/\rho_b = 2.4$ ) of the density ratios [in Figs. 5(c) and 5(d)] irrespective of the values of frequency ratios ( $f_n/f_f < 1$  or  $f_n/f_f > 1$ ). These observations of the flame dynamics in the phase space suggest that the response of the flame to the periodic forcing is asymmetric for the values of lower density ratios ( $\rho_u/\rho_b = 1.7$  and 1.9), where the unforced reacting flow dynamics is globally unstable.<sup>1</sup> On the contrary, such a behaviour of the flame dynamics is relatively symmetric for the intermediate ( $\rho_u/\rho_b = 2$ ) and the higher ( $\rho_u/\rho_b = 2.4$ ) density ratios, where the unforced reacting flow dynamics is observed to be intermittent and convectively unstable, respectively.<sup>1,34</sup> This behaviour of flame dynamics is, however, expected in convectively unstable cases due to the symmetric nature of the forcing.<sup>2</sup>

The qualitative observations of the symmetry in the forced flame response during off-resonance conditions at different density ratios (as shown in Fig. 5) further motivate us to quantify this symmetry aspect using a framework of synchronization. Here, we turn our attention to characterize the phase-locking behaviour of the local heat release rate fluctuations obtained from top and bottom branches of the flame with the forcing signal. In doing so, we calculate the instantaneous phases of these signals from an analytic signal approach based on the Hilbert transform.<sup>47</sup> The analytic signal ( $\zeta(t)$ ) is a complex quantity, where the real part is the original signal ( $x(t)$ ) and the imaginary part is the Hilbert transform of  $x(t)$ , i.e.,

$$H[x(t)] = P.V. \cdot \pi^{-1} \int_{-\infty}^{\infty} \frac{x(\tau)}{(t-\tau)} d\tau. \quad (4)$$

Therefore, the analytic signal is defined by  $\zeta(t) = x(t) + iH[x(t)] = A(t)e^{i\phi(t)}$ . Here,  $\phi(t)$  is the instantaneous phase and  $A(t)$  is the instantaneous amplitude of the signal. The mean frequency of the signal is then calculated as  $\omega = \langle d\phi/dt \rangle$ . In the Hilbert transform, the integral is

evaluated for the Cauchy principal value (P.V.). The instantaneous relative phase between the signals is calculated as  $\Delta\phi_{1,2}(t) = \phi_1(t) - \phi_2(t)$ . The condition for phase locking (or synchronization) is given by  $|\phi_1(t) - \phi_2(t)| \leq \text{constant}$ . During this condition, if the signals are contaminated with noise, the plot of the relative phase will show fluctuations around a constant phase difference; otherwise, it will be a straight horizontal line. When the signals are desynchronized, the relative phase between them will be unbounded and exhibits a continuous increase or decrease (depending on whether  $\omega_1$  is greater or lesser than  $\omega_2$ ) with time. This condition is known as phase drifting in the synchronization literature.<sup>47</sup> The instantaneous phase calculated from the Hilbert transform will have a physical meaning only if the governing signal is a narrowband and the representation of this signal in the analytic plane has a proper center of rotation.<sup>66</sup>

Figures 6(I) and 6(II) show two different ways of representing the spectral properties of the signals, where Fig. 6(I) corresponds to a time-frequency plot based on the wavelet transform and Fig. 6(II) demonstrates the amplitude spectrum of the signal obtained from the fast Fourier transform. Here, we use the continuous wavelet transform<sup>67</sup> (CWT) to represent the localized time varying frequency content of the heat release rate signal. The mathematical formula to calculate CWT is given by<sup>68</sup>

$$W(s, t_0) = \int_{-\infty}^{\infty} x(t) \Psi_{s,t_0}^*(t) dt, \quad (5)$$

where  $x(t)$  is the signal and  $\Psi_{s,t_0}^*(t)$  represents the complex conjugate of the mother wavelet function,  $\Psi_{s,t_0}(t)$ . Here,  $\Psi_{s,t_0}(t) = \frac{1}{\sqrt{s}} \Psi_0(\frac{t-t_0}{s})$ , wherein  $s$  is the time scale that determines the width of  $\Psi_0$  and  $t_0$  is the time shift of the wavelet function.

We use a complex Morlet wavelet<sup>68</sup> as the mother wavelet for our analysis. The Morlet wavelet is the most common mother wavelet function used in the analysis of practical sinusoidal signals. The complex nature of this wavelet

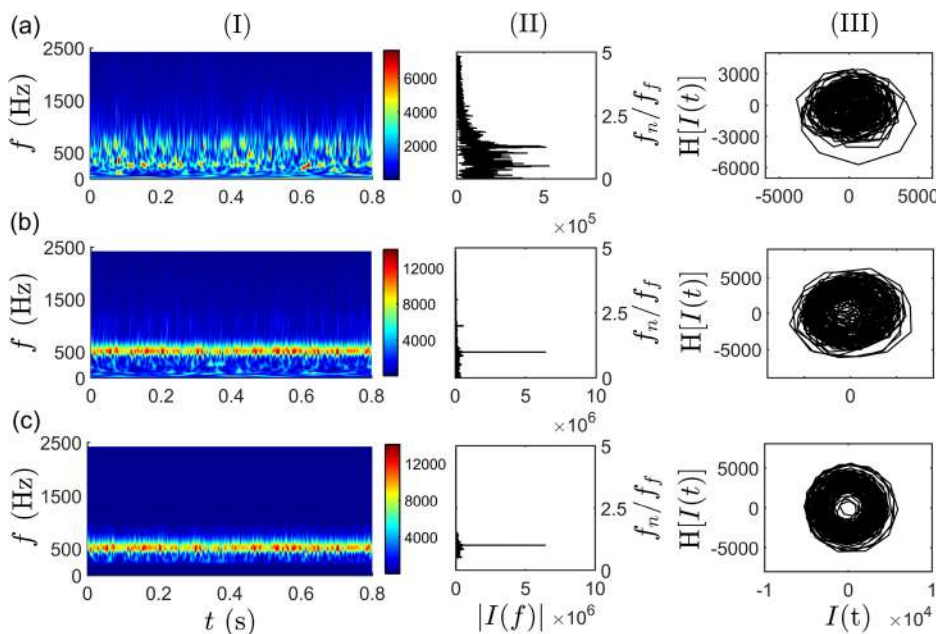


FIG. 6. (I) Time-frequency plot obtained from wavelet transform, (II) amplitude spectrum obtained from Fourier transform, and (III) analytic plane representation of the signal. These plots demonstrate the different properties of local heat release rate fluctuations obtained from the bottom half of the flame (I) for different conditions: (a) unforced ( $A_f=0$ ), (b) forced at high amplitude ( $A_f=0.02$ ), and (c) filtered signal corresponding to the forced state. The conditions that are fixed are  $x/D = 3$ ,  $U_{lip} = 35$  m/s,  $f_n/f_f < 1$ , and  $\rho_u/\rho_b = 1.7$ . The forcing frequency ( $f_f$ ) is fixed at 515 Hz. The frequency range chosen for bandpass filtering of the heat release rate signals is  $0.5f_f < f_f < 1.5f_f$ .

further helps in separating the instantaneous phase and amplitude information from the signal, which is not feasible with the real-valued wavelet functions. The mathematical form of the Morlet wavelet can be given as

$$\Psi_0(\eta) = \frac{1}{\sqrt[4]{\pi}} \exp(j\omega_0\eta) \exp(-\eta^2/2), \quad (6)$$

where  $\omega_0$  is a wavenumber and  $\eta$  is a non-dimensional time parameter. The smallest value of the scale ( $s_0$ ) is chosen as the integer multiples of  $dt = 1/(\text{sampling frequency})$ , and the largest value of the scale is chosen as  $J = \delta_j^{-1} \log_2(N\delta t/s_0)$ . Thus, the variation of the scale of the Morlet wavelet is given by  $s_j = s_0 2^{j\delta_j}$ , where  $j = 0, 1, 2, \dots, J$ . The parameters of the wavelet which are considered fixed are  $\omega_0 = 6$ ,  $s_0 = 2dt$ , and  $\delta_j = 0.5$ .

The spectral properties of the unforced local heat release rate fluctuations obtained from the bottom half of the flame are shown in Figs. 6(a-I) and 6(a-II). These plots suggest that the heat release rate fluctuations observed during the unforced state are broadband. This wide distribution of frequencies is further reflected in the representation of the signal in its analytic plane (plot between  $I(t)$  and  $H[I(t)]$ ). In such a plane [Fig. 6(a-III)], the behaviour of the trajectory is seemingly irregular exhibiting multiple centers of rotations about its origin. In Figs. 6(b-I) and 6(b-II), the spectral properties of  $I$  corresponding to the situation of high amplitude forcing ( $A_f = 0.02$ ) are shown. When the amplitude of forcing is sufficiently large (observed as a sharp amplitude peak in the frequency spectrum), the spectral properties of the unforced signal get organized around the forcing frequency [as shown in Fig. 6(b-I)]. Even though the signal is forced at high amplitude [see Fig. 6(b-II)], the analytical plane corresponding to this signal [Fig. 6(b-III)] still shows multiple centers of rotation, which results in an improper definition of the instantaneous phase of the signal.

The application of filtering to the heat released rate signals within a frequency band of  $0.5f_f < f < 1.5f_f$  removes the multiple centers of rotation in the analytic plane. We note that the interpretation of synchronization behaviour of the forcing signal with that of the heat release rate fluctuations is sensitive to the size of the frequency band. The change in the frequency range might lead to additional phase slips in the relative phase plot of the two signals. Here, the phase slip is related to an increase in the value of the unwrapped relative phase of the signals by integer multiples of  $2\pi$ . Figures 6(c-I) and 6(c-II) depict the spectral properties of the bandpass signal. Bandpass filtering removes the noisy fluctuations associated with low and high frequency components (outside the selected frequency band) present in the signal. The removal of such frequencies smoothens the signal. The effect of filtering is clearly reflected in the representation of the signal in the analytic plane, where the plot [see Fig. 6(c-III)] shows a clear center of rotation, thus enabling a proper definition of the phase in the signal.

The synchronization behaviour of the filtered local heat release rate signal ( $I$ ) with the forcing signal ( $F$ ) is examined by computing the instantaneous phase difference [ $\Delta\phi_{F,I}(t) = \phi_F(t) - \phi_I(t)$ ] between them. The effect of external forcing

on the top and bottom branches of the flame is analyzed for three different conditions of the frequency ratios as (i)  $f_n < f_f$ , (ii)  $f_n \approx f_f$ , and (iii)  $f_n > f_f$  at a constant value of the forcing amplitude ( $A_f = 0.02$ ). This investigation is necessary to quantitatively detect the aspect of symmetry in the response dynamics obtained from both branches of the flame to the external forcing, as shown qualitatively in Fig. 5. Furthermore, we compare such a behaviour of the forced flame response for two different conditions of the density ratios, i.e.,  $\rho_u/\rho_b = 1.9$  and  $3.2$ . The density ratios are chosen such that the low density ratio ( $\rho_u/\rho_b = 1.9$ ) and high density ratio ( $\rho_u/\rho_b = 3.2$ ) correspond to the globally unstable and convectively unstable modes, respectively.<sup>1</sup>

The quantitative analysis of the response of the top and bottom branches of the flames to the forcing, calculated in terms of the instantaneous phase difference, is shown in Fig. 7. We note that the heat release rate fluctuations obtained from the top branch of the flame exhibit phase drifting behaviour [see Fig. 7(a)], whereas that corresponding to the bottom branch of the flame is perfectly phase-locked with the forcing signal [see Fig. 7(b)]. The increasing trend in the plot of the instantaneous relative phase [Fig. 7(a)] suggests that the mean frequency ( $f_n$ ) of the heat release rate fluctuations is lesser than the forcing frequency, i.e.,  $f_n/f_f < 1$ . Here, the phase difference is calculated between the instantaneous phases of the forcing signal with that of the natural oscillations of the local heat release rate in the flame. When the value of flow velocity is such that  $f_n/f_f \approx 1$  [Figs. 7(c) and (d)], we witness the perfect locking of the instantaneous phases of the signals obtained from both branches of the flame with the forcing signal. Conversely, when  $f_n/f_f > 1$ , we observe the switching of phase locking behaviour of the heat release rate fluctuations from the bottom to the top branch of the flame. In this condition, we observe that the top branch of the flame is perfectly phase-locked with the forcing [Fig. 7(e)], while the bottom branch of the flame shows a phase drifting behavior [Fig. 7(f)]. The decreasing trend of the instantaneous relative phases in the plot further validates the condition of  $f_n/f_f > 1$  [see Fig. 7(f)]. This suggests that the response of two branches of the flames to the symmetric longitudinal forcing is asymmetric during off-resonance conditions of the frequency ratios, for the case of low density ratios. In such a situation, external forcing sheds synchronized vortices from the (bottom or top) lip of the bluff body, depending on whether  $f_n/f_f < 1$  or  $f_n/f_f > 1$ , respectively.

Figure 8 shows the temporal variation of the instantaneous phase difference of the local heat release rate fluctuations obtained from the top and bottom branches of the flame with the forcing signal, for three different conditions of the frequency ratios, i.e.,  $f_n/f_f < 1$  [Figs. 8(a) and 8(b)],  $f_n/f_f \approx 1$  [Figs. 8(c) and 8(d)], and  $f_n/f_f > 1$  [Figs. 8(e) and 8(f)]. We notice that, during all conditions of the frequency ratios, the instantaneous phase difference of the heat release rate fluctuations of both branches of the flame displays a perfect phase locking with the forcing signal. This observation of the relative phase further suggests that the effect of forcing is nearly symmetric on both branches of the flame during the high density ratio case. Thus, in the case of high density

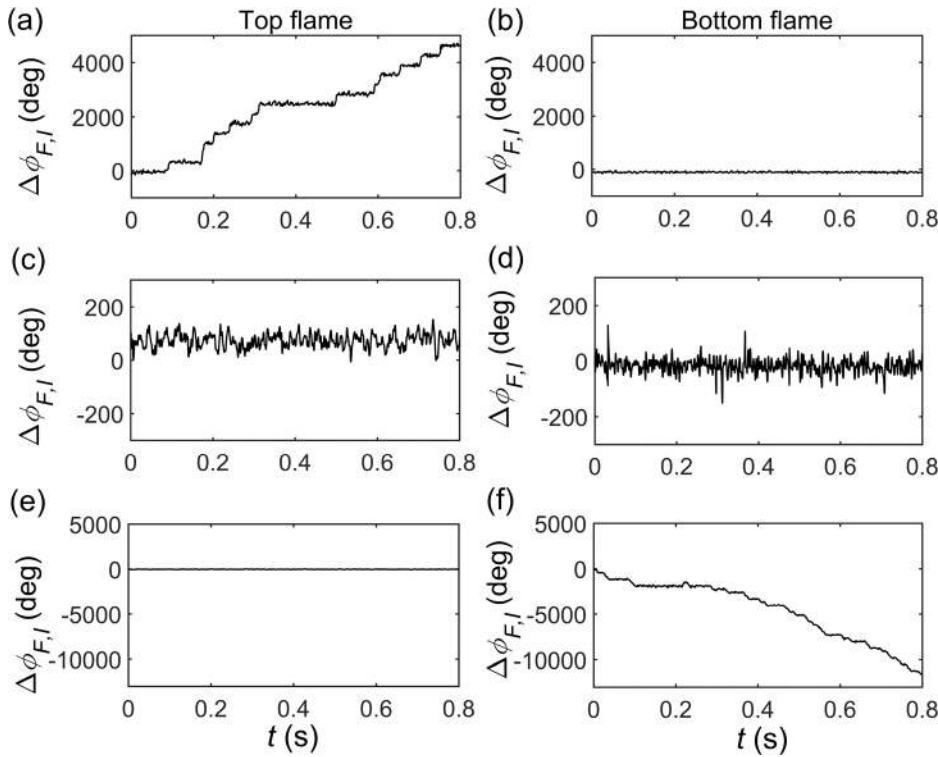


FIG. 7. The temporal variation of the relative phase of local heat release rate fluctuations obtained from the top and bottom branches of the flame with the external forcing for a low density case. The test conditions correspond to three values of the forcing frequency such that (a) and (b)  $f_n/f_f < 1$  ( $U_{lip} = 35$  m/s), (c) and (d)  $f_n/f_f \approx 1$  ( $U_{lip} = 41$  m/s), and (e) and (f)  $f_n/f_f > 1$  ( $U_{lip} = 46$  m/s). The parameters that are maintained constant are  $x/D = 3$ ,  $\rho_u/\rho_b = 1.9$ , and  $A_f = 0.02$ .

ratios, forcing simultaneously sheds a synchronized pair of vortices at the forcing frequency from the lip of both sides of the bluff body.

The low density ratio wakes, where the flow is globally unstable, exhibit a stronger sensitivity to the frequency ratio ( $f_n/f_f$ ). We notice that, when the density ratio is low (Fig. 7), the maximum amplitude of the acoustic perturbations considered in the present study is insufficient to simultaneously synchronize the heat release rate fluctuations obtained from

both branches of the flame with the forcing signal. Conversely, for the case of high density ratios (Fig. 8), this value of the forcing amplitude is sufficiently high to synchronize the instantaneous phases of the heat release rate fluctuations obtained from both branches of the flame with the forcing signal. Previous studies<sup>2,44</sup> on the same experimental dataset have not noticed the sensitivity of the low density ratio flame asymmetry to  $f_n/f_f$ . Specifically, the asymmetry exhibits phase synchronization of the bottom flame branch

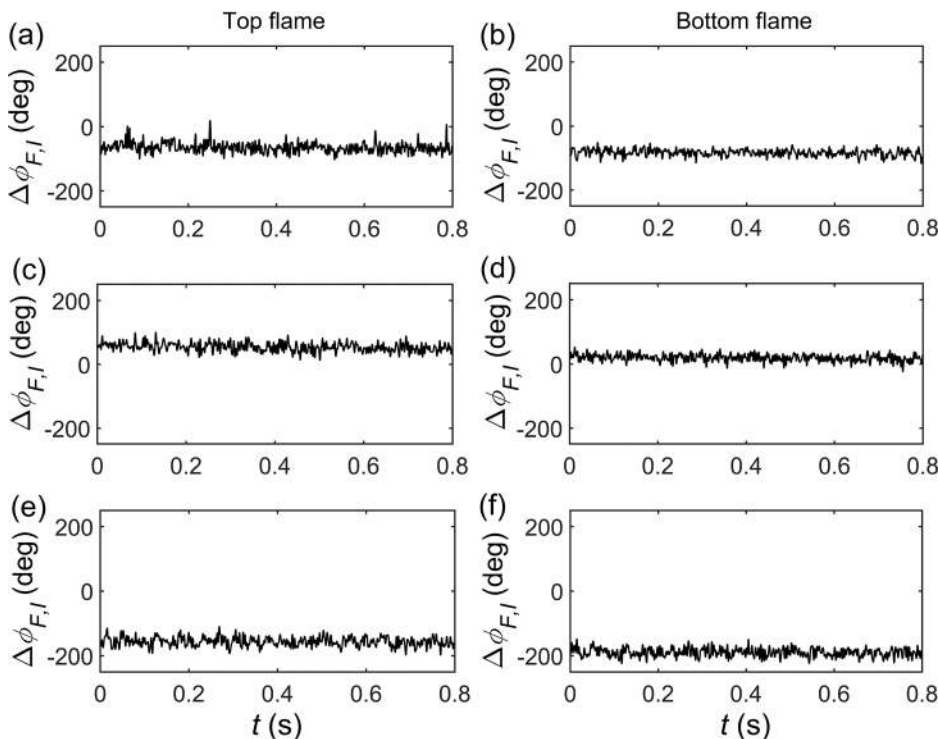


FIG. 8. The temporal variation of the relative phase of the local heat release rate fluctuations obtained from top and bottom branches of the flame with the external forcing for a high density case. The test conditions correspond to three values of the forcing frequency such that (a) and (b)  $f_n/f_f < 1$  ( $U_{lip} = 24$  m/s), (c) and (d)  $f_n/f_f \approx 1$  ( $U_{lip} = 41$  m/s), and (e) and (f)  $f_n/f_f > 1$  ( $U_{lip} = 44$  m/s). The parameters that are maintained constant are  $x/D = 3$ ,  $\rho_u/\rho_b = 3.2$ , and  $A_f = 0.02$ .

when  $f_n/f_f < 1$  and phase synchronization of the top flame branch when  $f_n/f_f > 1$ .

In the case of intermediate density ratios, i.e.,  $\rho_u/\rho_b = 2$  or 2.2, we notice a perfect phase locking of top and bottom branches of the flame with the forcing signal, irrespective of whether  $f_n/f_f < 1$  or  $f_n/f_f > 1$ . The results for these density ratios are similar to that observed for the high density ratio case ( $\rho_u/\rho_b = 3.2$ ), as shown in Fig. 8. Emerson and Lieuwen<sup>1</sup> and Suresha *et al.*<sup>34</sup> have reported the presence of intermittency during  $\rho_u/\rho_b = 2$  and showed that the features of such intermittent oscillations vanish at  $\rho_u/\rho_b = 2.4$ . Intermittency, here, refers to the apparently random switching of the flow dynamics from a region of convectively unstable (features of a high density ratio) to a globally unstable (features of a low density ratio) mode of oscillations. Thus, during  $\rho_u/\rho_b = 2$ , we expect that the phase-locking behaviour of the top and bottom branches of the flame will have features that are observed in Figs. 7 and 8 for different conditions of the frequency ratios. That is, when the intermittent flow dynamics exhibit a globally unstable behavior, an asymmetry in the phase locking behaviour of both branches of the flame is expected to occur. Conversely, when the intermittent flow dynamics exhibit a convectively unstable behavior, the perfect phase locking of both branches of the flame is expected to happen. However, we do not observe such features at this density ratio or at the other intermediate density ratio of  $\rho_u/\rho_b = 2.2$ . This might be because the maximum amplitude of forcing used in all the experiments is high enough to diminish such expected features of the phase dynamics during intermediate density ratios and responsible for the entrainment of the phases of both branches of the flame with the forcing signal.

### C. Characterization of phase-locking behavior between top and bottom branches of the flame

We now move our attention to investigate the phase locking behaviour between the heat release rate signals

obtained from the top and bottom branches of the flame. This analysis, in turn, helps in quantifying the relative phase between the vortices that are shed from the top and bottom sides of the bluff body during a high Reynolds number flow condition. This also helps in identifying the kind of vortex shedding pattern (sinuous or varicose) exhibited by the bluff body wake at a given density ratio. During the sinuous type of vortex shedding, both branches of the flame move in the same direction such that the relative phase between the oscillations of their edges is close to  $0^\circ$  or the relative phase between the fluctuations of their local heat release rate is close to  $180^\circ$ . The opposite happens for the varicose mode of vortex shedding.<sup>2</sup> Figure 9 shows the temporal variation of the phase difference between the heat release rate fluctuations obtained from the top and bottom branches of the flame for different density ratios. The flow velocity (hence, the mean frequency of natural oscillations of the flame) and the amplitude of forcing are maintained constant at  $U_{lip} = 41$  m/s and  $A_f = 0.02$ , respectively. The choice of  $U_{lip}$  is such that the mean frequency of the unforced natural oscillations in the local heat release rate fluctuations is nearly the same as the frequency of the external forcing (i.e.,  $f_n/f_f \approx 1$ ).

In order to detect synchrony between the heat release rate signals of the top and the bottom branches of the flame, we compute the instantaneous phase difference between them [i.e.,  $\Delta\phi_{T,B}(t) = \phi_T(t) - \phi_B(t)$ , where  $T$  and  $B$  correspond to the top and the bottom branches of the flame, respectively]. We notice that for  $A_f = 0.02$ , as the forcing amplitude is sufficiently high and since  $f_n/f_f \approx 1$ , the instantaneous phases of the heat release rate fluctuations obtained from both branches of the flame are perfectly phase locked. This phase locking is confirmed from the fluctuations of the relative phase of these signals around a constant phase shift [refer to insets of Figs. 9(a)–9(c)]. In Figs. 9(a)–9(c), we plot the histogram of the relative phase wrapped in the interval of  $-180^\circ$  to  $+180^\circ$ . We observe that, for the case of low density

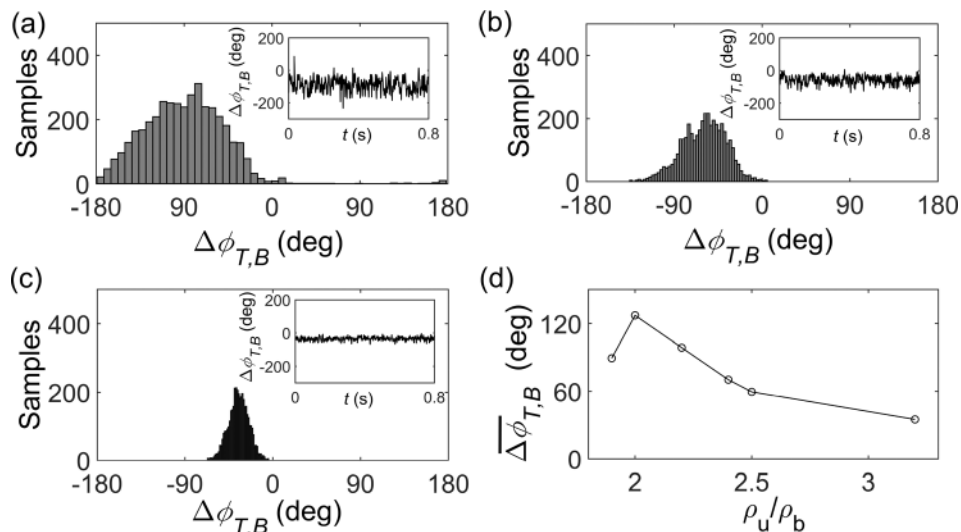


FIG. 9. (a)–(c) The distribution and the temporal variation (in insets) of the instantaneous phase difference between the signals of heat release rate fluctuations obtained from top and bottom branches of the flame for three different conditions of density ratios as  $\rho_u/\rho_b = 1.9, 2.5$ , and  $3.2$ , respectively. (d) The plot showing the variation of the mean relative phase angle between the top and bottom branches of a reacting wake with different values of the density ratio, i.e.,  $\rho_u/\rho_b = 1.9, 2, 2.2, 2.4, 2.5$ , and  $3.2$ . The parameters that are fixed are  $U_{lip} = 41$  m/s,  $f_n/f_f \approx 1$ ,  $A_f = 0.02$ , and  $x/D = 3$ . During  $f_n/f_f \approx 1$ , the flame dynamics is such that both branches of the flame are perfectly the phase locked state with each other [see insets of (a)–(c)].

ratios [shown in Fig. 9(a)], the histogram of the relative phase displays a wider distribution, whereas that of the higher density ratio [shown in Fig. 9(c)] shows a narrower distribution. On the other hand, for an intermediate case of the density ratio [Fig. 9(b)], the width of the distribution is in between the value observed for the cases of low and high density ratios. The observation of the narrow distribution in the relative phase, for the high density ratio case, demonstrates that the cycle-to-cycle variation of instantaneous phases of the heat release rate fluctuations obtained from both branches of the flame is very low. In contrast, this cycle-to-cycle variation of instantaneous phases of the heat release rate signals is high during the low density ratio case. This further supports the observation that the low density ratio flames are less receptive to external forcing than high density ratio flames.<sup>27</sup>

Figure 9(d) shows the variation in the mean phase difference ( $\overline{\Delta\phi} = \frac{1}{N} \sum_{i=1}^N \Delta\phi_i$ ) between the signals of heat release rate fluctuations obtained from the top and bottom branches of the flame, for different values of the density ratios. The value of flow velocity is maintained such that  $f_n/f_f \approx 1$ . We observe that with an increase in the density ratio, the mean relative phase between the top and bottom branches of the flame shows a monotonic decrease after a small initial increase in the plot. This indicates that the increase in the preheating temperature of the reactant mixture changes the relative shedding frequency of the vortex from the top and bottom edges of the bluff body. This change follows the transition of the vortex shedding pattern from the predominantly sinusoidal (phase difference  $\geq 90^\circ$ ) to the predominantly varicose (phase difference  $\leq 90^\circ$ ) mode.<sup>2</sup>

Furthermore, we compare the influence of external forcing on the phase locking behaviour of the heat release rate signals obtained from both branches of the flame for different locations along the flame length. In order to do this, we quantify the relative phase between these signals acquired at three different locations of the flame such as  $x/D = 3, 5$ , and

7 for  $\rho_u/\rho_b = 1.9$  [Figs. 10(a)–10(c)] and 3.2 [Figs. 10(d)–10(f)]. We notice that, in the near field of the bluff body wake, as shown in Figs. 10(a) and 10(d), the relative phase shows fluctuations around a constant phase shift (i.e., a perfect phase-locking condition). Nevertheless, as we move away from near field of the bluff body [shown in Figs. 10(b), 10(c), 10(e), and 10(f)], the relative phase shows multiple phase slips depicting the lack of perfect synchronization between these signals. This indicates that the response of the flame dynamics to the external perturbations weakens as we move away from the bluff body location. We notice that the lack of synchrony observed in the flame response is more for the high density ratio case compared to the low density ratio case, as the number of phase slips is more and less for the former and latter cases in the plot of relative phase, respectively. Thus, it is to be noted that the detection of phase locking between the signals obtained from the top and bottom branches of the flame is highly dependent on the choice of the flame location.

Lastly, we examine the variation of recurrence properties such %RR and %DET of the local heat release rate fluctuations obtained from the top and the bottom branches of the flame, at various distances downstream of the bluff body, for different values of the forcing amplitude. In Fig. 11, we plot the variation of these recurrence measures for the top [Figs. 11(a) and 11(b)] and the bottom [Figs. 11(c) and 11(d)] sides of the flame separately, when  $\rho_u/\rho_b = 2$ . We notice the variation in the values of these measures for both sides of the flame with an increase in the forcing amplitudes. For the top side of the flame [Fig. 11(a)], the values of %RR display an increasing trend for  $x/D = 3, 4$ , and 5, and this remains nearly the same for  $x/D = 6, 7$ , with an increase in the forcing amplitude, whereas, in Fig. 11(b), we notice a continuous increase in the values of %DET with the forcing amplitude for all locations along the flame length. Furthermore, the value of %DET is observed to decrease at a particular forcing amplitude with the increase in the distance

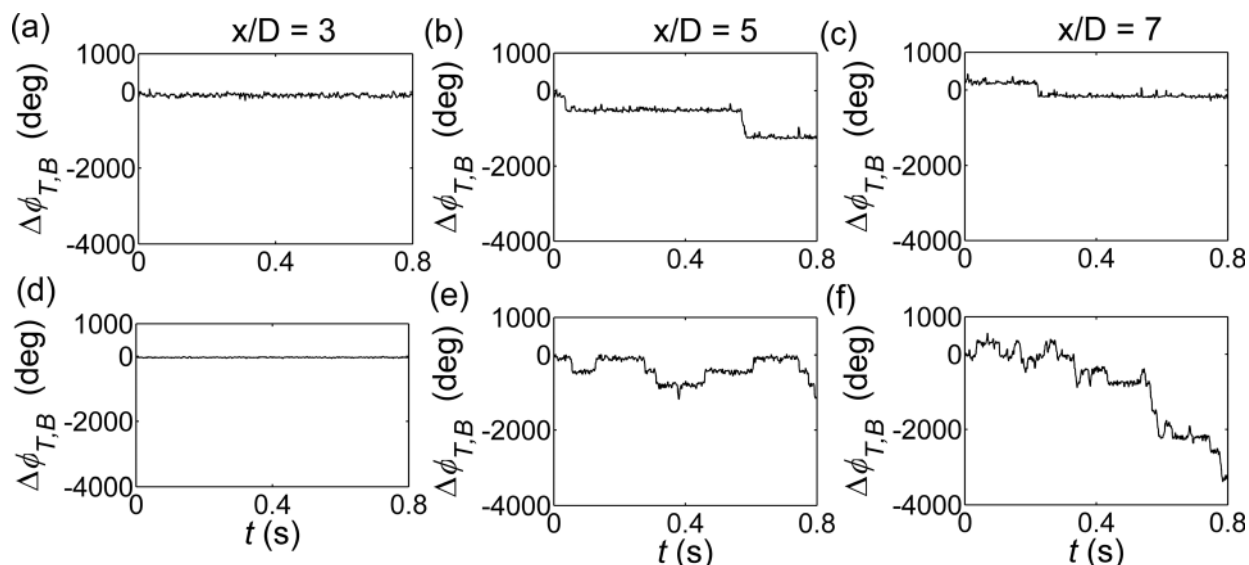


FIG. 10. The plots of the relative phase between the local heat release rate fluctuations obtained from the top and bottom branches of the flame at three different locations along the flame length as  $x/D = 3, 5$ , and 7, for two different values of the density ratios (a)–(c)  $\rho_u/\rho_b = 1.9$  and (d)–(f)  $\rho_u/\rho_b = 3.2$ . The parameters that are fixed are  $U_{lip} = 41$  m/s,  $f_n/f_f \approx 1$ , and  $A_f = 0.02$ .

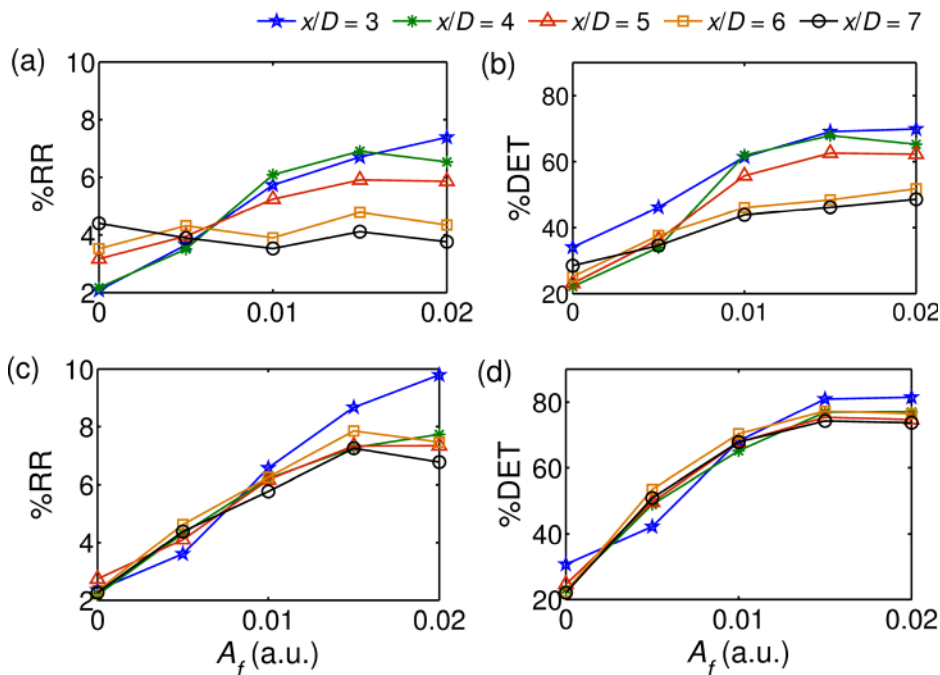


FIG. 11. The variation of recurrence quantities  $\%RR$  and  $\%DET$  for (a) and (b) top and (c) and (d) bottom sides of the flame with different values of forcing amplitudes obtained at various locations along the flame length. The flame distances are  $x/D = 3, 4, 5, 6,$  and  $7$ , and the forcing amplitude values are  $A_f = 0, 0.005, 0.01, 0.015,$  and  $0.02$ . The conditions that are fixed are  $\rho_u/\rho_b = 2, U_{lip} = 40$  m/s, and  $f_n/f_f \approx 1$ .

along the flame length. This reasserts that the response of oscillations in the top side of the flame to the forcing decreases (hence, there is a decrease in the periodicity of oscillations) as we move away from the bluff body location. The opposite behaviour is observed in the oscillations of bottom side of the flame, where we notice a near collapse of all the plots of recurrence measures,  $\%RR$  [Fig. 11(c)] and  $\%DET$  [Fig. 11(d)], obtained for different locations along the flame length with an increase in the forcing amplitude. This suggests that the response of forcing is nearly the same along the length of the bottom side of the flame. The application of forcing periodically sheds vortices from the bluff body; however, the persistence of these vortices along the flame length is asymmetric for both sides of the bluff body. In particular, at the density ratio of 2 and when the frequency ratio is such that  $f_n/f_f \approx 1$ , we observe that the structures shed from the top side of the bluff body lose coherence faster than those shed from the bottom side. Thus, even though the application of external forcing is symmetric in the system, the response of the system dynamics to the forcing may not be always symmetric and is highly dependent on the various factors such as the geometry of the system and conditions of the underlying hydrodynamic field and those of the external forcing.

#### IV. CONCLUSIONS

This paper describes the study of the forced response of a longitudinally excited reacting wake for different density and excitation frequency ratios. By using tools from nonlinear dynamics, we show that the dynamics of the local heat release rate fluctuations during the unforced state have low determinism, and the value of this determinism gradually increases with an increase in the forcing amplitude. We further characterize the symmetry of forced flame response by computing the instantaneous relative phases of the local heat release rate fluctuations obtained from the top and the bottom

branches of the flame with the forcing signal. We observe that, for the low density ratio case, when  $f_n < f_f$ , the bottom branch of the flame exhibits more receptivity to forcing and gets easily phase-locked. In contrast, the top branch of the flame oscillations displays a weak response to forcing and does not get phase-locked with the forcing signal. The reverse happens when  $f_n > f_f$ , i.e., the top branch of the flame oscillations shows a perfect phase-locking with forcing and not the bottom branch of the flame oscillations. In the case of high density ratios, the effect of forcing is nearly the same for all conditions of forcing ( $f_f < f_n$  or  $f_f > f_n$ ), where both (top and bottom) branches of the flame show a perfect phase-locking with the forcing signal. This observation is explored in detail in Ref. 2 from the viewpoint hydrodynamics and is characterized here using a dynamical systems theory.

By comparing the instantaneous phase difference between the top and bottom branches of the flame, when  $f_f \approx f_n$ , we notice that the mean phase difference between the top and bottom branches of the flame decreases from a high value close to  $130^\circ$  to a low value close to  $35^\circ$  with an increase in the density ratio. This results in the transition of the vortex shedding pattern from a sinuous (predominantly asymmetric) to a varicose (predominantly symmetric) mode. The distribution of the relative phase between the top and bottom branches of the flame is narrower for the high density ratio case, as compared to the broader distribution observed for the low density ratio case. This suggests that the globally unstable low density ratio reacting wakes are more resistant to the harmonic forcing than the high density ratio convectively unstable reacting wakes as the correlation in phases between the signals is weaker for the former and stronger for the latter.

#### ACKNOWLEDGMENTS

S. A. Pawar and R. I. Sujith are thankful to the Indian Institute of Technology Madras (IITM) and Office of Naval Research Global (ONRG) for their financial support.

- <sup>1</sup>B. Emerson, J. O'Connor, M. Juniper, and T. Lieuwen, *J. Fluid Mech.* **706**, 219 (2012).
- <sup>2</sup>B. Emerson and T. Lieuwen, *J. Fluid Mech.* **779**, 716 (2015).
- <sup>3</sup>H. Y. Ken, A. Trouvé, and J. W. Daily, *J. Fluid Mech.* **232**, 47 (1991).
- <sup>4</sup>P. Langhorne, *J. Fluid Mech.* **193**, 417 (1988).
- <sup>5</sup>S. Menon and W.-H. Jou, *Combust. Sci. Technol.* **75**, 53 (1991).
- <sup>6</sup>K. Schadow, E. Gutmark, T. Parr, D. Parr, K. Wilson, and J. Crump, *Combust. Sci. Technol.* **64**, 167 (1989).
- <sup>7</sup>S. J. Shanbhogue, S. Husain, and T. Lieuwen, *Prog. Energy Combust. Sci.* **35**, 98 (2009).
- <sup>8</sup>D. A. Smith and E. E. Zukoski, "Combustion instability sustained by unsteady vortex combustion," AIAA Paper No. 85-1248, 1985.
- <sup>9</sup>T. J. Poinso, A. C. Trouve, D. P. Veynante, S. M. Candel, and E. J. Esposito, *J. Fluid Mech.* **177**, 265 (1987).
- <sup>10</sup>T. C. Lieuwen, *Unsteady Combustor Physics* (Cambridge University Press, 2012).
- <sup>11</sup>C. H. Williamson, *Annu. Rev. Fluid Mech.* **28**, 477 (1996).
- <sup>12</sup>K. Schadow and E. Gutmark, *Prog. Energy Combust. Sci.* **18**, 117 (1992).
- <sup>13</sup>J. W. S. Rayleigh, *Nature* **18**, 319 (1878).
- <sup>14</sup>S. A. Pawar, A. Seshadri, V. R. Unni, and R. I. Sujith, *J. Fluid Mech.* **827**, 664–693 (2017).
- <sup>15</sup>S. Mondal, V. R. Unni, and R. Sujith, *J. Fluid Mech.* **811**, 659 (2017).
- <sup>16</sup>R. Sujith, M. Juniper, and P. Schmid, *Int. J. Spray Combust. Dyn.* **8**, 119 (2016).
- <sup>17</sup>S. Ducruix, T. Schuller, D. Durox, and S. Candel, *J. Propul. Power* **19**, 722 (2003).
- <sup>18</sup>T. C. Lieuwen and V. Yang, *Progress in Astronautics and Aeronautics* (American Institute of Aeronautics and Astronautics (AIAA), 2005).
- <sup>19</sup>A. Bourehla and F. Baillot, *Combust. Flame* **114**, 303 (1998).
- <sup>20</sup>S. Ducruix, D. Durox, and S. Candel, *Proc. Combust. Inst.* **28**, 765 (2000).
- <sup>21</sup>T. Schuller, D. Durox, and S. Candel, *Combust. Flame* **134**, 21 (2003).
- <sup>22</sup>H. Santosh, T. Lieuwen *et al.*, *J. Propul. Power* **24**, 1390 (2008).
- <sup>23</sup>C. Nottin, R. Knikker, M. Boger, and D. Veynante, *Proc. Combust. Inst.* **28**, 67 (2000).
- <sup>24</sup>D. H. Shin, D. V. Plaks, T. Lieuwen, U. M. Mondragon, C. T. Brown, and V. G. McDonnell, *J. Propul. Power* **27**, 105 (2011).
- <sup>25</sup>J. O'Connor and T. Lieuwen, *Combust. Sci. Technol.* **183**, 427 (2011).
- <sup>26</sup>B. Emerson, U. Mondragon, V. Acharya, D. H. Shin, C. Brown, V. McDonnell, and T. Lieuwen, *Combust. Sci. Technol.* **185**, 1056 (2013).
- <sup>27</sup>P. Huerre and P. A. Monkewitz, *Annu. Rev. Fluid Mech.* **22**, 473 (1990).
- <sup>28</sup>A. Perry, M. Chong, and T. Lim, *J. Fluid Mech.* **116**, 77 (1982).
- <sup>29</sup>A. Prasad and C. H. Williamson, *J. Fluid Mech.* **333**, 375 (1997).
- <sup>30</sup>P. McMurtry, J. Riley, and R. Metcalfe, *J. Fluid Mech.* **199**, 297 (1989).
- <sup>31</sup>S. M. Bush and E. J. Gutmark, *AIAA J.* **45**, 662 (2007).
- <sup>32</sup>M. H. Yu and P. A. Monkewitz, *Phys. Fluids A: Fluid Dyn.* **2**, 1175 (1990).
- <sup>33</sup>R. Erickson and M. Soteriou, *Combust. Flame* **158**, 2441 (2011).
- <sup>34</sup>S. Suresha, R. Sujith, B. Emerson, and T. Lieuwen, *Phys. Rev. E* **94**, 042206 (2016).
- <sup>35</sup>M. Masselin and C.-M. Ho, in *Shear Flow Control Conference* (1985), p. 571.
- <sup>36</sup>B. D. Bellows, A. Hreiz, and T. Lieuwen, *J. Propul. Power* **24**, 628 (2008).
- <sup>37</sup>R. Bishop and A. Hassan, *Proc. R. Soc. London, Ser. A* **277**, 51–75 (1964).
- <sup>38</sup>Y. Tanida, A. Okajima, and Y. Watanabe, *J. Fluid Mech.* **61**, 769 (1973).
- <sup>39</sup>O. M. Griffin and S. E. Ramberg, *J. Fluid Mech.* **75**, 257 (1976).
- <sup>40</sup>R. D. Blevins, *Flow-Induced Vibration* (Van Nostrand Reinhold Co., Inc., New York, NY, USA, 1990).
- <sup>41</sup>J. Sheridan, J. Carberry, J.-C. Lin, and D. Rockwell, *J. Fluids Struct.* **12**, 215 (1998).
- <sup>42</sup>J. Carberry, J. Sheridan, and D. Rockwell, *J. Fluid Mech.* **538**, 31 (2005).
- <sup>43</sup>C. Barbi, D. Favier, C. Maresca, and D. Telionis, *J. Fluid Mech.* **170**, 527 (1986).
- <sup>44</sup>B. Emerson, J. O'Connor, D. Noble, and T. Lieuwen, "Frequency locking and vortex dynamics of an acoustically excited bluff body stabilized flame," AIAA Paper No. 2012-0451, 2012.
- <sup>45</sup>H. D. Abarbanel, R. Brown, J. J. Sidorowich, and L. S. Tsimring, *Rev. Mod. Phys.* **65**, 1331 (1993).
- <sup>46</sup>N. Marwan, M. C. Romano, M. Thiel, and J. Kurths, *Phys. Rep.* **438**, 237 (2007).
- <sup>47</sup>A. Pikovsky, M. Rosenblum, and J. Kurths, *Synchronization: A Universal Concept in Nonlinear Sciences* (Cambridge University Press, 2003), Vol. 12.
- <sup>48</sup>A. Balanov, N. Janson, D. Postnov, and O. Sosnovtseva, *Synchronization: From Simple to Complex* (Springer, 2009), Vol. 17.
- <sup>49</sup>S. Shanbhogue, D. H. Shin, S. Hemchandra, D. Plaks, and T. Lieuwen, *Proc. Combust. Inst.* **32**, 1787 (2009).
- <sup>50</sup>T. Lieuwen and Y. Neumeier, *Proc. Combust. Inst.* **29**, 99 (2002).
- <sup>51</sup>L. K. Li and M. P. Juniper, *J. Fluid Mech.* **726**, 624 (2013).
- <sup>52</sup>L. K. Li and M. P. Juniper, *J. Fluid Mech.* **735**, R5 (2013).
- <sup>53</sup>L. K. Li and M. P. Juniper, *Proc. Combust. Inst.* **34**, 947 (2013).
- <sup>54</sup>S. Balusamy, L. K. Li, Z. Han, M. P. Juniper, and S. Hochgreb, *Proc. Combust. Inst.* **35**, 3229 (2015).
- <sup>55</sup>S. Chaudhuri, S. Kostka, M. W. Renfro, and B. M. Cetegen, *Combust. Flame* **157**, 790 (2010).
- <sup>56</sup>S. Chaudhuri, S. Kostka, S. G. Tuttle, M. W. Renfro, and B. M. Cetegen, *Combust. Flame* **158**, 1358 (2011).
- <sup>57</sup>F. Takens *et al.*, *Lecture Notes Math.* **898**, 366 (1981).
- <sup>58</sup>A. M. Fraser and H. L. Swinney, *Phys. Rev. A* **33**, 1134 (1986).
- <sup>59</sup>M. B. Kennel, R. Brown, and H. D. Abarbanel, *Phys. Rev. A* **45**, 3403 (1992).
- <sup>60</sup>J. P. Eckmann, S. O. Kamphorst, and D. Ruelle, *EPL (Europhys. Lett.)* **4**, 973 (1987).
- <sup>61</sup>T. Aparicio, E. F. Pozo, and D. Saura, *J. Econ. Behav. Org.* **65**, 768 (2008).
- <sup>62</sup>N. Marwan, N. Wessel, U. Meyerfeldt, A. Schirdewan, and J. Kurths, *Phys. Rev. E* **66**, 026702 (2002).
- <sup>63</sup>C. L. Webber and J. P. Zbilut, *J. Appl. Physiol.* **76**, 965 (1994).
- <sup>64</sup>L. Trulla, A. Giuliani, J. Zbilut, and C. Webber, *Phys. Lett. A* **223**, 255 (1996).
- <sup>65</sup>J. Hołyst, M. Żebrowska, and K. Urbanowicz, *Eur. Phys. J. B* **20**, 531 (2001).
- <sup>66</sup>T. Yalçınkaya and Y. C. Lai, *Phys. Rev. Lett.* **79**, 3885 (1997).
- <sup>67</sup>M. Farge, *Annu. Rev. Fluid Mech.* **24**, 395 (1992).
- <sup>68</sup>C. Torrence and G. P. Compo, *Bull. Am. Meteorol. Soc.* **79**, 61 (1998).
- <sup>69</sup>S. Mondal, S. Pawar, and R. Sujith, *Chaos: An Interdiscip. J. Nonlinear Sci.* **27**, 103119 (2017).